

## MIT Open Access Articles

### *Dynamic speckle illumination wide-field reflection phase microscopy*

The MIT Faculty has made this article openly available. **Please share** how this access benefits you. Your story matters.

**Citation:** Choi, Youngwoon et al. "Dynamic Speckle Illumination Wide-Field Reflection Phase Microscopy." *Optics Letters* 39, 20 (October 2014): 6062 © 2014 Optical Society of America

**As Published:** <http://dx.doi.org/10.1364/OL.39.006062>

**Publisher:** Optical Society of America

**Persistent URL:** <http://hdl.handle.net/1721.1/119870>

**Version:** Author's final manuscript: final author's manuscript post peer review, without publisher's formatting or copy editing

**Terms of use:** Creative Commons Attribution-Noncommercial-Share Alike





Published in final edited form as:

*Opt Lett.* 2014 October 15; 39(20): 6062–6065.

## Dynamic speckle illumination wide-field reflection phase microscopy

Youngwoon Choi<sup>1,\*</sup>, Poorya Hosseini<sup>1</sup>, Wonshik Choi<sup>2</sup>, Ramachandra R. Dasari<sup>1</sup>, Peter T. C. So<sup>1,3</sup>, and Zahid Yaqoob<sup>1</sup>

<sup>1</sup>Laser Biomedical Research Center, G. R. Harrison Spectroscopy Laboratory, Massachusetts Institute of Technology, Cambridge, Massachusetts 02139, USA

<sup>2</sup>Department of Physics, Korea University, Seoul 136-701, South Korea

<sup>3</sup>Department of Mechanical and Biological Engineering, Massachusetts Institute of Technology, Cambridge, Massachusetts 02139, USA

### Abstract

We demonstrate a quantitative reflection-phase microscope based on time-varying speckle-field illumination. Due to the short spatial coherence length of the speckle field, the proposed imaging system features superior lateral resolution, 520 nm, as well as high-depth selectivity, 1.03  $\mu\text{m}$ . Off-axis interferometric detection enables wide-field and single-shot imaging appropriate for high-speed measurements. In addition, the measured phase sensitivity of this method, which is the smallest measurable axial motion, is more than 40 times higher than that available using a transmission system. We demonstrate the utility of our method by successfully distinguishing the motion of the top surface from that of the bottom in red blood cells. The proposed method will be useful for studying membrane dynamics in complex eukaryotic cells.

---

Quantitative phase imaging (QPI) is a technique for accurately measuring the structure and function of transparent biological samples without requiring exogenous contrast agents [1]. In the last few years, QPI has proven to be a powerful tool for label-free quantification of pathophysiological processes at the single-cell level [2,3]. In particular, QPI systems have been used to study fast ( $> 100$  Hz) dynamics of membrane motion in biological cells. Normally transmission phase images are acquired in time, and the measured phase variations are converted into height fluctuations. The phase measurements in transmission, however, do not decouple the physical thickness from refractive index variations in samples.

In contrast, configurations relying on reflection measurements have certain advantages. The interpretation of the measured reflection phase does not require the knowledge of refractive index distribution within the sample as long as we are interested in the outermost surface morphology. In addition, the reflection measurement provides  $2n/n$  higher phase sensitivity compared to its transmission counterpart, where  $n$  is the refractive index of the host medium and  $n$  is the refractive index difference between the sample and the medium [4]. Since

water-based host media are usually used in most cases,  $n$  is typically 1.33, and  $n$  ranges from 0.03 to 0.06 for most biological samples [5]. Thus more than an order-of-magnitude phase gain, which can be up to about 90 for eukaryotic cells, can be easily achieved using reflection-type QPI configurations.

To take advantage of higher sensitivity of reflection phase measurements, the prerequisite is to attain depth selectivity. A general approach is to utilize a broadband light source and produce a temporal coherence gate at the target position. Using this strategy, light arriving from depths out of the coherence gate region can be effectively rejected [6–8]. Our lab has also demonstrated a single-shot wide-field reflection phase microscope based on temporal gating. The demonstrated axial resolution, however, was limited (several microns) due to rather narrow bandwidth of the source [4]. Yamauchi et al. have achieved higher axial resolution,  $\sim 1 \mu\text{m}$ , by using a white-light illumination [9]. Their instrument, however, is not appropriate for high-speed ( $>100 \text{ Hz}$ ) phase measurements since it requires multiple interferograms to obtain a single-reflection phase image.

Another approach to achieve depth sectioning is through complex speckle-field illumination. In the past, speckle fields have been mainly used to reduce noise and improve lateral resolution via coherent or incoherent averaging of multiple measurements [10–12]. Although single-shot full-field interferometric confocal imaging has also been demonstrated [13], the demonstrated spatial resolution has been limited to several microns. The enhancement of depth resolution assisted by the decorrelation nature of a speckle field has also been demonstrated via time-varying speckle-field in conjunction with interferometric detection [14]. However, the achieved depth resolution was again limited due to lack of speckle overlap as a result of reference wavefront tilt for off-axis configuration. Recently, we resolved this limitation by using a grating to form an off-axis setup (in transmission mode configuration) without physical tilting of the reference beam [15]. In this Letter, we present a wide-field reflection phase microscope based on dynamic speckle illumination that features single-shot quantitative phase measurements with high lateral and axial resolution. The quick decorrelation nature of 3D speckle-fields allows us to achieve confocal equivalent depth selectivity. We call this method speckle-correlation reflection phase microscopy (SpeCRPM).

The experimental setup is depicted in Fig. 1(a). A mode-locked Ti:sapphire laser (Mira 900, Coherent) with a center wavelength of  $\lambda_0 = 800 \text{ nm}$  and spectral width  $\Delta\lambda \approx 17 \text{ nm}$  is used as a light source. The collimated laser beam illuminates a rotating ground glass diffuser (D: DG1200, Thorlabs), which generates a dynamically varying speckle field. After passing through a polarizer P0, which defines an input polarization state for maximum interference, the speckle field is split into sample and reference beams via a polarizing beam splitter (PBS). A half-wave plate (HWP) is placed before the PBS to either balance or redistribute the input power in the two arms. A Linnik-type interferometer is constructed using two objective lenses in conjunction with two quarterwave plates (QWPs), one in each arm. The image of the diffuser is projected onto the object and reference mirror planes via two  $4f$  imaging configurations that share the three lenses before the PBS and employ two matching objectives (1.0 NA,  $60\times$ , water immersion, Olympus), one in each arm. A mirror (M) is placed at the focal plane of the reference arm. During setup alignment and characterization,

a separate mirror is used as an object. The retardation axes of the QWPs are set so that the returning light from each arm is perpendicularly polarized to itself. Consequently, the returning beams are steered to the output port of the PBS with polarizations orthogonal to that of each other. For off-axis holography, a grating (G: Ronchi Rulings, Edmund Optics) is positioned at the first intermediate plane. To minimize aberrations introduced by different pathways through the optics, the zeroth-order beam is blocked and only the +1st and -1st diffraction orders are selected to pass. Since each of the diffracted orders contains both the sample and reference beams, two cross polarizers are placed in the Fourier plane (one in front of each diffraction order) to allow only one beam (sample or reference) to pass through. A CMOS camera (Flea3, Point Grey) is placed in the image plane such that both the object and the grating are in focus simultaneously. Another polarizer at 45° orientation is introduced in front of the camera to achieve interference between the orthogonally polarized sample and reference beams. For a stationary diffuser, a typical speckle pattern from the reference mirror is as shown in Fig. 1(b). For zero optical path-length difference (OPD) between the two arms, the sample speckle pattern shows a fairly good match with that from the reference arm as presented in Fig. 1(c). When the two speckle fields combine at the camera plane, an interference pattern (straight fringes) appears in addition to the speckle distribution as shown in Fig. 1(d). Furthermore, the interference fringes stay stationary and are not affected by different speckle patterns introduced by the diffuser. Therefore, when the diffuser is rotated fast enough within the camera exposure time, sufficiently large number of speckle patterns are generated and averaged out during the signal acquisition. In our experiment, the typical rotational speed of the diffuser is about 500–600 rpm, which generates about 400 different speckles within a 10 ms exposure time. This is 4–7 times larger than the minimum number of speckles required to average out the speckle-induced intensity variations [10,11]. When the local speckle formation is washed out, a clear interference pattern as shown in Fig. 1(e) becomes readily available for recording. When imaging a sample (biological or otherwise) with a nonplanar morphology, the interference pattern is modified accordingly such that it bears the information of the sample morphology as well as dynamics. By analyzing the measured single-shot interferograms, both the amplitude and phase information of the sample can be obtained [16,17].

The generated speckle field is composed of multiple plane waves illuminating the sample at various oblique angles limited by the numerical aperture (NA) of the objective lens. Thus the lateral resolution of SpeCRPM is twice as good as that available with coherent illumination. The spatial resolution of SpeCRPM is equivalent to the mean speckle size produced at the sample plane. We have quantified this parameter by measuring the autocorrelation length of the speckle field. From the sample speckle distribution shown in Fig. 1(c), we have calculated the autocorrelation function along lateral directions as shown in Fig. 2(a); the inset shows the corresponding 2D autocorrelation map. The full-width-half-maximum (FWHM) of the autocorrelation is measured to be 520 nm, which is in good agreement with the value predicted by Van Cittert–Zernike theorem [18].

To demonstrate lateral resolution of SpeCRPM, we imaged polystyrene beads (Polyscience, Inc.) on a glass plate. The 750-nm-diameter beads used for imaging formed several clusters in the field of view. First, the beads sample was illuminated with a plane wave. The measured amplitude image is shown in Fig. 2(c). Since the diffraction-limited resolution of

this coherent imaging is  $1.22\lambda_0/NA_{\text{det}} = 980$  nm, where  $NA_{\text{det}}$  is the detection NA, multiple adjacent beads were not distinguishable due to the lack of resolving power. Next, the same site was imaged using the dynamic speckle illumination. Now the diffraction limited resolution of the system is expected to be  $1.22\lambda_0/(NA_{\text{ill}} + NA_{\text{det}}) = 490$  nm, which was verified by the autocorrelation measurement as discussed above;  $NA_{\text{ill}}$  is the illumination NA. Figure 2(d) shows the corresponding amplitude image using the dynamic speckle illumination where the individual beads are now clearly distinguishable. Furthermore, Fig. 2(b) shows the profiles along the dotted lines in Figs. 2(c) and 2(d).

Since the speckle distribution generated by the diffuser is 3D, the correlation along the axial direction quickly decays similar to that in the case of lateral directions. If the position of the sample mirror varies, for example, by  $1\ \mu\text{m}$  from the zero OPD position, the speckle distribution changes significantly as shown in Fig. 3(b). The resulting interference pattern, as shown in Fig. 3(c), is neither straight fringes nor stationary for varying speckle patterns. The interference contrast, therefore, substantially drops when different speckle patterns are averaged, as shown in Fig. 3(d). We have systematically investigated achievable optical sectioning via speckle correlation. Multiple interference images were acquired at different axial positions of the sample mirror. To determine the fringe contrast, complex amplitude maps were computed, converted into intensity images, and then averaged over the whole field-of-view. As shown in Fig. 3(e), the depth sectioning is about  $6\ \mu\text{m}$  for plane-wave illumination, which is mainly determined by the coherence length of the light source. Note that the mode-locked laser was used only because it offered more power required for obtaining enough reflection signal from biological samples. With the dynamic speckle illumination, however, the correlation length is significantly reduced. The FWHM of axial correlation was measured to be  $1.03\ \mu\text{m}$ , which is fairly close to the confocal limit of the objective lens. A similar decorrelation effect resulting from speckle formation was also observed when using a CW laser [15]. Since SpeCRPM does not require reference mirror tilt for off-axis configuration, a uniform interference contrast can be obtained over the entire field-of-view up to the maximum illumination NA.

Next, we used healthy red blood cells (RBCs) to demonstrate depth-resolved phase measurements in biological samples. Since the typical thickness of RBCs is about  $2\text{--}3\ \mu\text{m}$ , SpeCRPM successfully distinguishes each surface, top as well as bottom, due to its superior axial resolution. When the focus is placed at the bottom surface, the signal is dominantly generated from the glass substrate on which the RBC is rested. Figures 4(a) and 4(b) show the amplitude and phase images, respectively, of an RBC in double-pass mode. The actual phase map can be obtained by dividing the total measured phase by 2.

However, when the focus is placed on the top surface of the RBC, the signal from the bottom surface is effectively rejected due to optical sectioning. Figures 4(c) and 4(d) show the reflectance and phase maps, respectively, of the top surface. Since only the phase with certain strength of reflection signal is reliable, the measured phase from locations with corresponding amplitude below a certain threshold value is not considered. Furthermore, as there is no phase reference associated with the empty region, the overall phase offset in Fig. 4(d) was removed by subtracting the mean value. We note that the reflection phase image in

Fig. 4(d) is attributed to the surface morphology of the RBC, and not to the phase retardation due to the refractive index contrast.

Since SpeCRPM offers single-shot and wide-field imaging, it is capable of high-speed reflection phase measurements. Multiple interferograms were acquired for a total of 10 s at 100 fps, which was limited only by the camera speed. If we were to increase the camera speed further, we would need to speed up the diffuser rotation proportionally to achieve the same speckle decorrelation effect and hence image quality. Corresponding phase maps were computed by analyzing the measured interferograms. Figure 4(e) shows the measured phase fluctuations at a lateral position indicated by an arrow for both top (reflection measurement) and bottom (double-pass transmission measurement) surfaces. The black line shows the phase jittering measured without any sample. The rms amplitude of this empty fluctuation is 5.2 mrad, representing the system stability. The blue line shows the time-varying phase measured in double-pass transmission mode. The rms amplitude of the fluctuation is 32.4 mrad, which corresponds to RBC thickness variation of 34.4 nm; here the refractive index difference  $n$  is assumed to be 0.06. In this case, the measurement sensitivity is determined to be 0.94 mrad/nm. In contrast, the phase fluctuation measured in reflection mode is shown by the red line. The rms amplitude of the fluctuation is 533 mrad, which corresponds to the motion of the top surface by 25.5 nm. We note that this measurement does not require the knowledge of the refractive index of the sample. The measured phase sensitivity is 20.9 mrad/nm, which is 22 times better than that of the double-pass transmission measurement. When compared with a typical single-pass transmission phase imaging setup, SpeCRPM has an additional factor of 2 phase measurement sensitivity.

In conclusion, we have demonstrated a wide-field reflection- phase microscope based on dynamic speckle illumination. The depth selectivity of our setup is determined by the speckle decorrelation as a function of optical path length. Due to the short correlation length of the speckle field along the axial direction, 1.03  $\mu\text{m}$  depth selectivity was achievable. Furthermore, due to the short autocorrelation length of the speckle-field, the proposed wide-field reflection-phase microscope offers superior lateral resolution as well as significantly reduced diffraction noise. With the improved depth selectivity, we have successfully distinguished and quantified the motion of a top surface of a healthy red blood cell. The measurement sensitivity of our system is 44 times higher than that achievable with a typical transmission approach. Since this technique features single-shot high-speed phase measurements with improved sensitivity and axial sectioning, it will be useful in many biological studies including measurement of nuclear membrane stiffness in laminopathies.

## Acknowledgments

This work was supported by The National Institute of Biomedical Imaging and Bioengineering (grant no. 9P41EB015871), Hamamatsu Photonics (Japan), Korean Ministry of Science, ICT, and future planning (grant no. R2013080003), and Korea Health Industry Development Institute (grant no. HI14C1234).

## References

1. Ferraro, P.; Wax, A.; Zalevsky, Z., editors. *Coherent Light Microscopy: Imaging and Quantitative Phase Analysis*. 1st ed.. Springer; 2011.

2. Park YK, Diez-Silva M, Popescu G, Lykotrafitis G, Choi WS, Feld MS, Suresh S. *Proc. Natl. Acad. Sci. USA*. 2008; 105:13730. [PubMed: 18772382]
3. Shaked NT, Satterwhite LL, Telen MJ, Truskey GA, Wax A. *J. Biomed. Opt.* 2011; 16:030506. [PubMed: 21456860]
4. Yaqoob Z, Yamauchi T, Choi W, Fu D, Dasari RR, Feld MS. *Opt. Express*. 2011; 19:7587. [PubMed: 21503067]
5. Rappaz B, Marquet P, Cuche E, Emery Y, Depeursinge C, Magistretti P. *Opt. Express*. 2005; 13:9361. [PubMed: 19503137]
6. Choma MA, Ellerbee AK, Yang CH, Creazzo TL, Izatt JA. *Opt. Lett.* 2005; 30:1162. [PubMed: 15945141]
7. Joo C, Akkin T, Cense B, Park BH, de Boer JE. *Opt. Lett.* 2005; 30:2131. [PubMed: 16127933]
8. Sarunic MV, Weinberg S, Izatt JA. *Opt. Lett.* 2006; 31:1462. [PubMed: 16642139]
9. Yamauchi T, Iwai H, Yamashita Y. *Opt. Express*. 2011; 19:5536. [PubMed: 21445192]
10. Monroy F, Rincon O, Torres YM, Garcia-Sucerquia J. *Opt. Commun.* 2008; 281:3454.
11. Park Y, Choi W, Yaqoob Z, Dasari R, Badizadegan K, Feld MS. *Opt. Express*. 2009; 17:12285. [PubMed: 19654630]
12. Bianco V, Paturzo M, Finizio A, Balduzzi D, Puglisi R, Galli A, Ferraro P. *Opt. Lett.* 2012; 37:4212. [PubMed: 23073414]
13. Redding B, Bromberg Y, Choma MA, Cao H. *Opt. Lett.* 2014; 39:4446. [PubMed: 25078199]
14. Somekh MG, See CW, Goh J. *Opt. Commun.* 2000; 174:75.
15. Choi Y, Yang TD, Lee KJ, Choi W. *Opt. Lett.* 2011; 36:2465. [PubMed: 21725446]
16. Cuche E, Bevilacqua F, Depeursinge C. *Opt. Lett.* 1999; 24:291. [PubMed: 18071483]
17. Ikeda T, Popescu G, Dasari RR, Feld MS. *Opt. Lett.* 2005; 30:1165. [PubMed: 15945142]
18. Saleh, BEA.; Teich, MC. *Fundamentals of Photonics*. 2nd ed.. Wiley Series in Pure and Applied Optics (Wiley-Interscience); 2007. p. 433

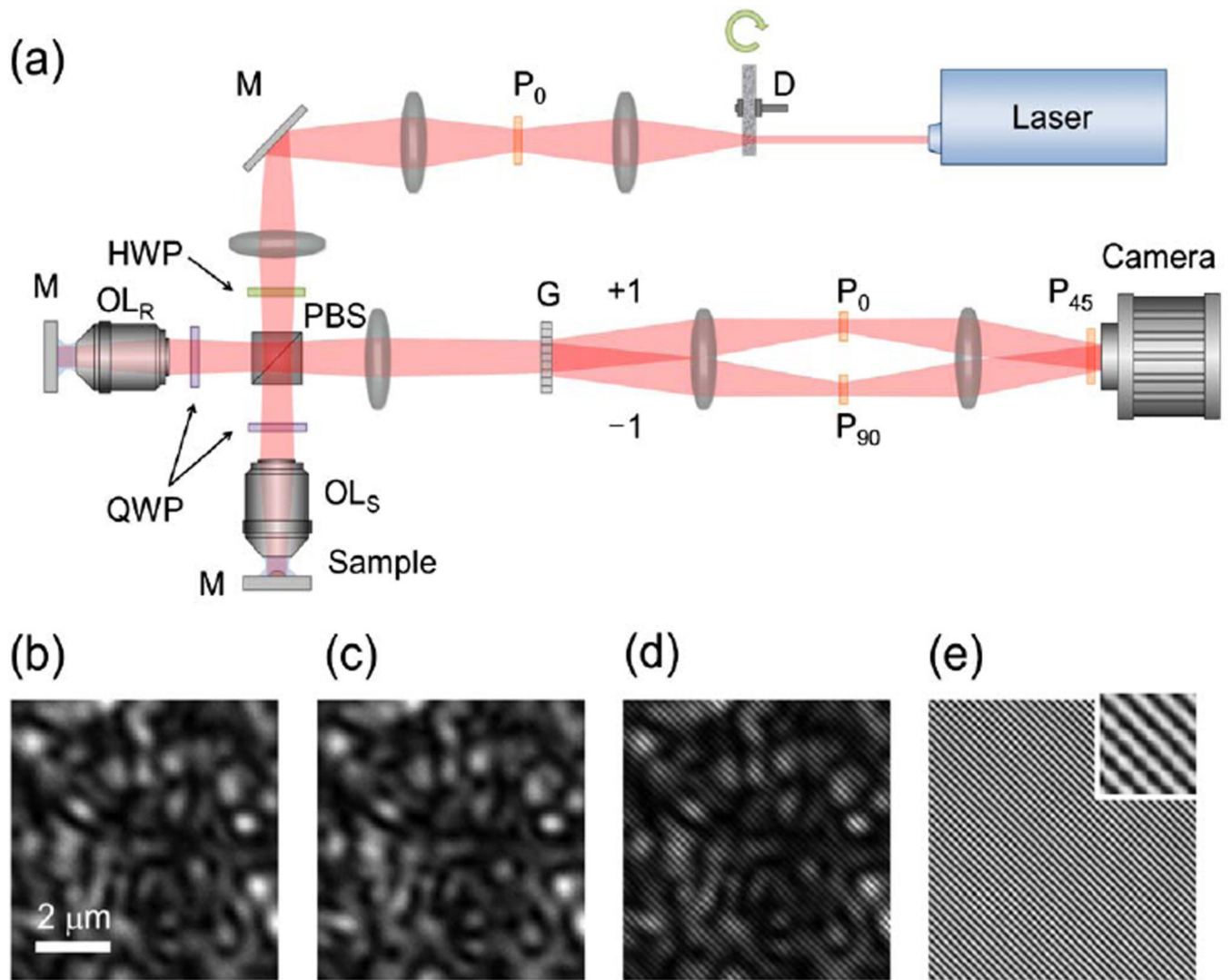


**Fig. 1.**

(a) Schematic diagram of the experimental setup. D, diffuser; M, mirror; PBS, polarizing beam splitter; HWP, half-wave plate; QWP, quarter-wave plate;  $OL_R$  and  $OL_S$ , objective lenses for reference and sample arms; G, grating;  $P_\alpha$ , polarizer with  $\alpha$ -deg rotation. Multiple diffraction orders generated by G except  $\pm 1$  are omitted. (b), (c) Intensity distribution of the speckle field from reference and sample arms, respectively, with no path length difference. (d), (e) Interference pattern at the camera with stationary and rotating diffuser, respectively. Inset is  $3\times$  zoom view of the interference.



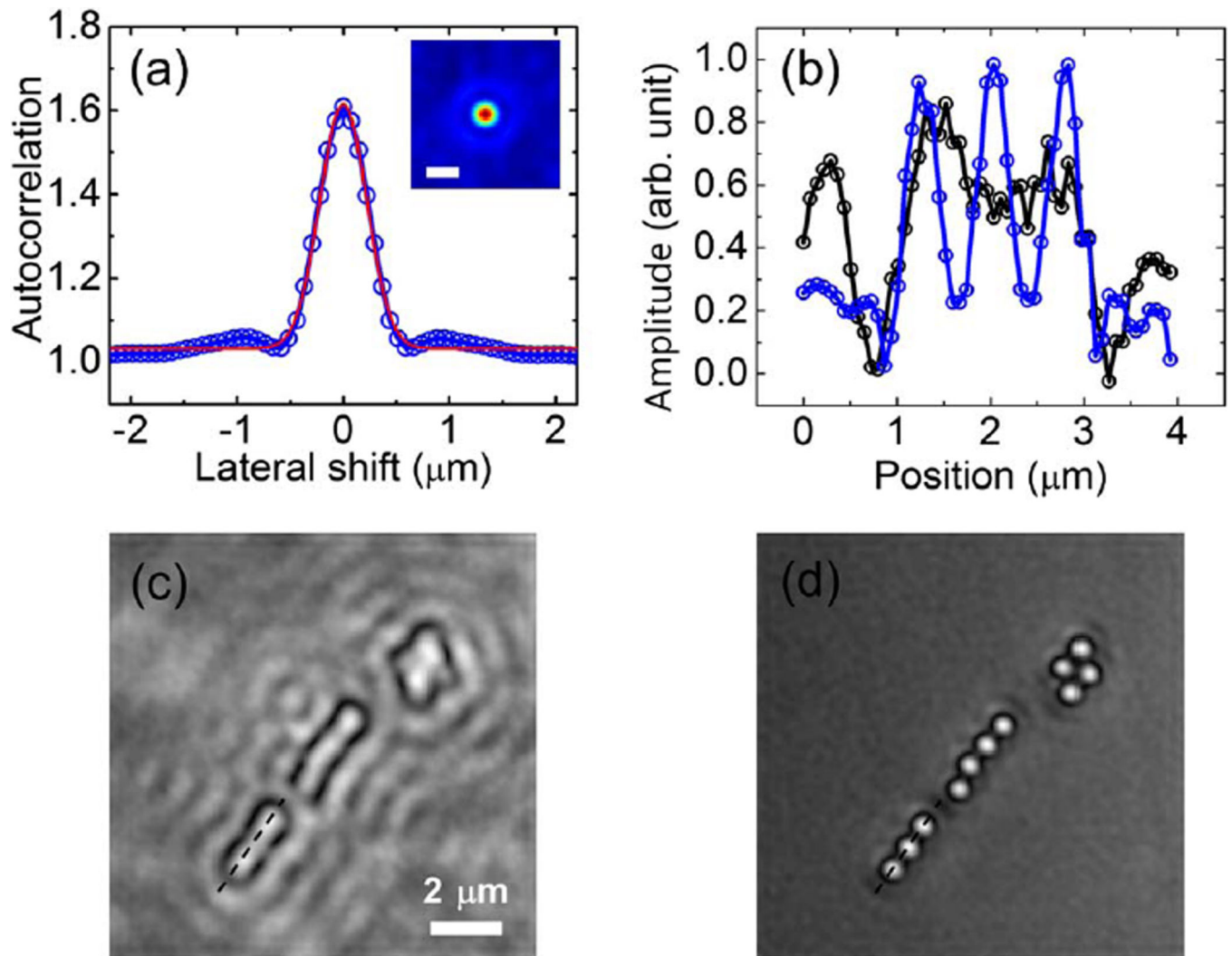


**Fig. 2.**

(a) Section profile of the autocorrelation map obtained from the speckle distribution in the sample plane. The FWHM of Gaussian fit, represented with a red line, is 520 nm. The inset shows the 2D autocorrelation map. Scale bar: 1  $\mu\text{m}$ . (b) Section profiles of the bead cluster along the black dashed line in (c). Black and blue curves correspond to (c) and (d), respectively. (c), (d) Amplitude image of bead clusters on a glass substrate using plane-wave and dynamic speckle illuminations, respectively.

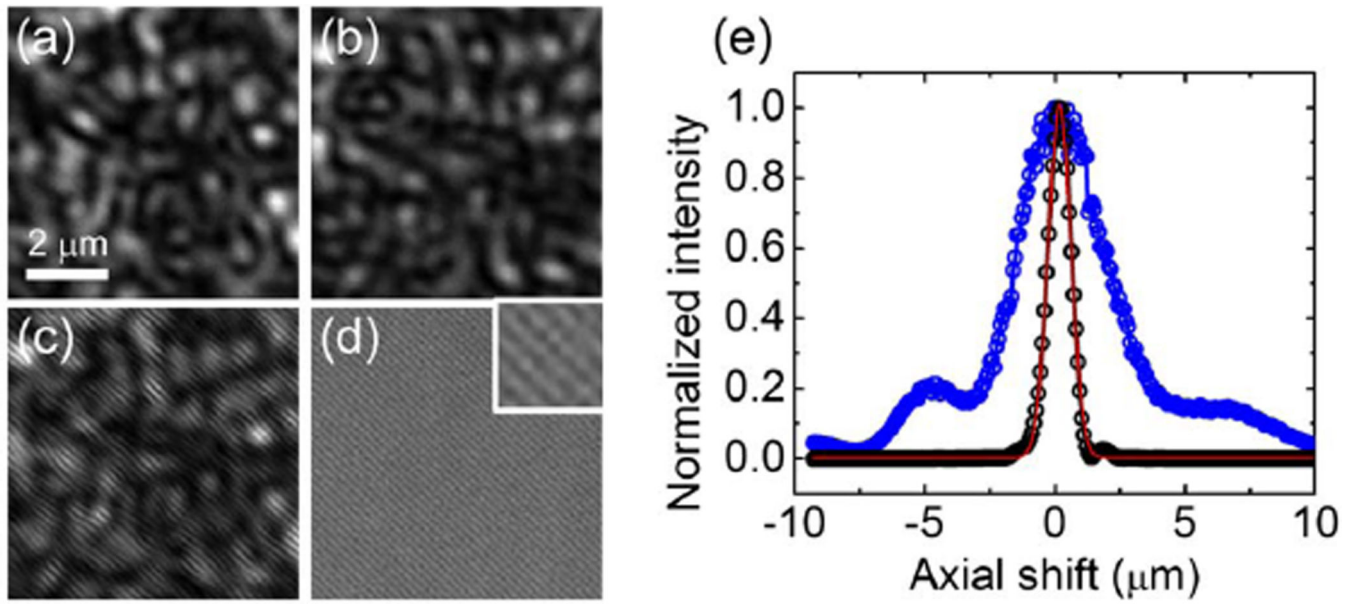


**Fig. 3.**

(a), (b) Speckle-field distributions at the camera from reference and sample arms, respectively, with  $1\ \mu\text{m}$  path-length difference. (c) Interference of the two speckle fields shown in (a) and (b) with a stationary diffuser. (d) Corresponding interference pattern at the camera plane with the spinning diffuser. Inset shows  $3\times$  zoom view of the interference. (e) Interference strength as a function of axial shift of the sample mirror; blue and black lines represent plane-wave and dynamic speckle illumination. The FWHM (using Gaussian fit), shown by the red line is  $1.03\ \mu\text{m}$  for the dynamic illumination case.

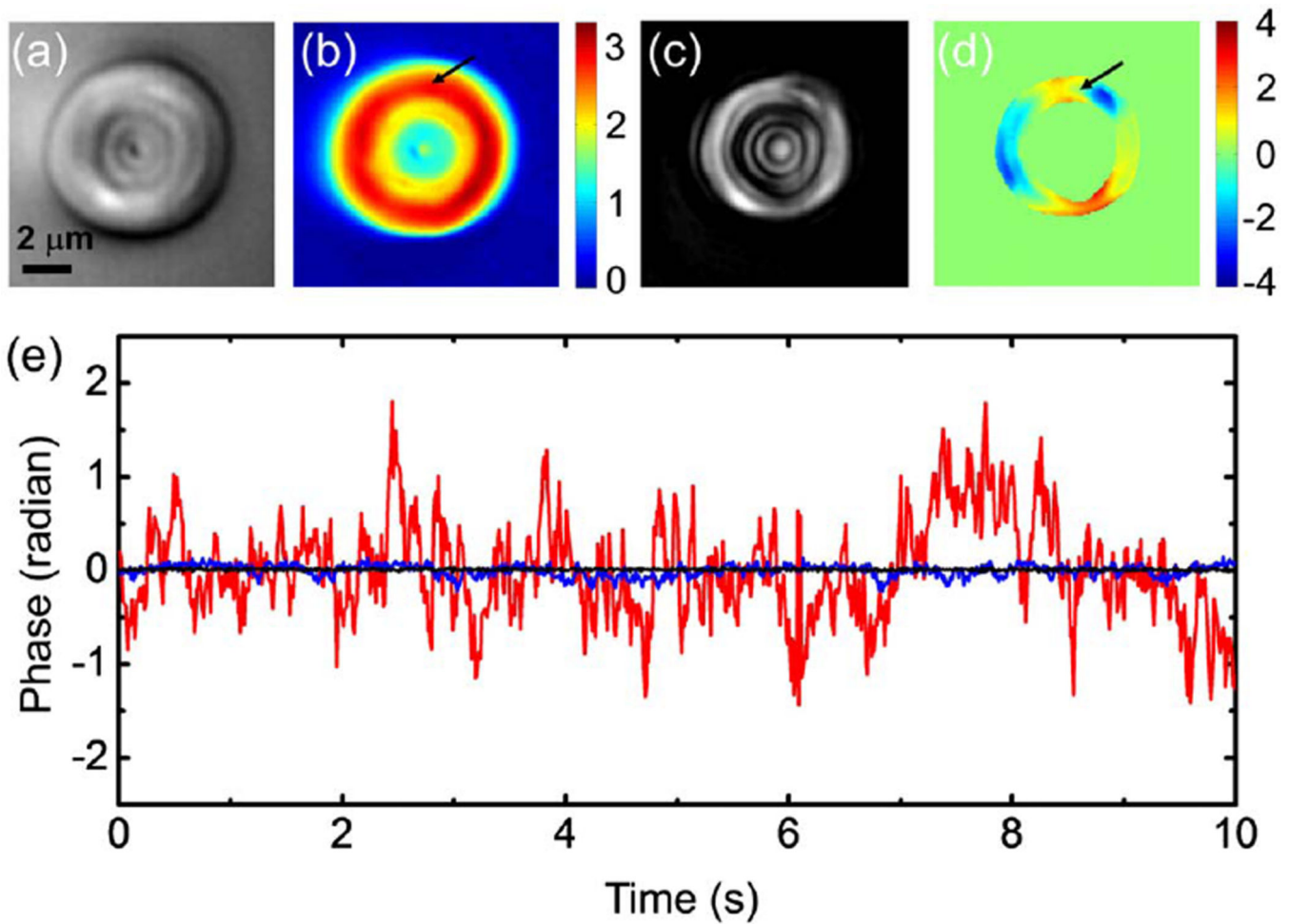


**Fig. 4.** (a), (b) Double-pass transmission images of an RBC for (a) amplitude and (b) phase, respectively. (c), (d) Reflection images of the same RBC for (c) amplitude and (d) corresponding phase image. Only the phase values corresponding to the region with strong reflection are shown. (e) Fluctuation of phase values. Blue line: transmission phase fluctuation measured at the point indicated by the arrow in (b). Red line: reflection phase fluctuation measured at the point indicated by an arrow in (d). Black line: background fluctuation. Scale bars in (b) and (d): phase in radians.